




Cite this: *Phys. Chem. Chem. Phys.*,
2020, 22, 20837

Characterization of plasma and gas-phase chemistry during boron-nitride nanomaterial synthesis by laser-ablation of boron-rich targets

Shurik Yatom * and Yevgeny Raitsev

In this work, solid targets made from boron and boron nitride (BN) materials are ablated by a nano-second pulsed laser at sub-atmospheric pressures of nitrogen and helium gases. The excited species in the ablation plume from the target are probed by spatiotemporally resolved optical emission spectroscopy (OES). The evaluation of the chemical composition of the plasma plume revealed that for both boron-rich targets, emission from BN molecules is always observed in nitrogen-rich environments. In addition, BN molecules are also present when ablating a boron nitride target in a helium gas environment, an indication that BN molecules in the plume may originate from the solid target. Furthermore, the ablation of the BN target features emission of B_2N molecules, regardless of the pressure and surrounding gas. These results suggest that the ablation of the BN target is more favorable for the generation of complex molecules containing boron and nitrogen species and possibly hint that BN is also more favorable feedstock for high-yield BN nanomaterial synthesis. Plasma parameters such as the electron temperature (peak value of 1.3 eV) and density (peak value of $2 \times 10^{18} \text{ cm}^{-3}$) were also investigated in this work in order to discuss the chemical dynamics in the plume.

Received 28th May 2020,
Accepted 12th August 2020

DOI: 10.1039/d0cp02890h

rsc.li/pccp

1. Introduction

Boron-nitride (BN) nanomaterials have attracted great interest due to their unique electrical, thermal and mechanical properties. Boron-nitride nanotubes (BNNTs) were predicted in 1994¹ and synthesized in 1995.² Since their discovery, BNNTs have invoked broad inter-disciplinary interest due to their vast potential in a wide variety of applications. The stiffness and strength of BNNTs allow the preparation of strong and lightweight composites that are capable of enduring high temperatures.^{3,4} BNNTs are electrical insulators with high thermal stability, therefore they are expected to be useful for thermal management in, for example, electronics,⁵ aerospace, *etc.* Studies showed that BN materials can be used as efficient, non-toxic catalysts.^{6,7} Optics and photonics are other areas where BNNTs have potential as light-emitting diodes and photodetectors with narrow wavelength selectivity for emission and detection.^{8,9} Other areas of potential applications for BNNTs include vibrational damping,^{10,11} piezo-electric¹² and hydrophobic materials,¹³ neutron sensing¹⁴ and shielding,¹⁵ and applications in oncology¹⁶ and drug delivery.¹⁷

The synthesis of BNNTs has been successfully demonstrated by a variety of techniques such as atmospheric pressure and high pressures arcs,^{18,19} laser ablation^{20–22} and inductively-coupled

plasma torches.^{23–25} However, physico-chemical mechanisms by which BNNTs are synthesized are not well understood. One possible mechanism is the so-called “root-growth” mechanism, which was proposed in the work of Arenal *et al.*²⁰ and further developed in the work listed in ref. 26. The “root-growth” mechanism requires the formation of a molten boron seed particle, boron droplet at a temperature above 2000 K, which is bombarded by nitrogen atoms and nitrogen-containing molecules, thereby sustaining the BNNT growth from the droplet. This mechanism presented evidence in post-run characterization of the synthesized products which revealed that BNNTs are connected to boron droplets.^{18,24} Other experiments and molecular dynamic (MD) simulations suggest that boron droplets are not necessary for the facilitation of BNNT synthesis in plasma.²⁷ Independent of the primary mechanism of the growth, their validation requires *in situ* characterization of synthesis processes.^{28–30}

During the plasma-based synthesis, the main plasma processes are ionization, dissociation, association, and recombination. Since plasma promotes various plasma-chemical reactions and processes, it is critically important to identify the gas phase/plasma phase precursors sustaining the growth. In molecular dynamics simulations, the synthesis of BNNTs and BN nanostructures was explored by means of boron droplet (at a temperature of 2000–2400 K) bombardment by nitrogen atoms,²⁶ BN molecules,³¹ synthesis from molecular precursors

Princeton Plasma Physics Laboratory, Princeton University, NJ, USA.
E-mail: syatom@pppl.gov

such as borazine ($B_3N_3H_6$) and iminoborane ($HBNH$),^{31,32} radical BN ³² with/without the addition of hydrogen and mixtures of B/N/H in different ratios.³² In experiments, the chemistry induced in plasmas that contain B and N species was probed by optical emission spectroscopy (OES) to survey the emission of species in laser ablation³³ and induction thermal plasma.²⁵ The OES results detected mainly BN , N_2 , N_2^+ , BH and NH molecules and their possible roles in the synthesis of BN films or nanotubes were discussed. Infrared spectroscopy of laser ablation of B targets in NH_3 showed the formation of complex species, including B_2N , iminoborane and borazine.³⁴

In a recent study on the gas composition for high temperature growth of BN nanomaterials,³⁵ the formation of different chemical species relies on using the thermodynamic approach of minimization of the Gibbs free energy.³⁶ The results showed that for B–N and B–N–H gas mixtures under thermodynamic equilibrium at pressures 1–10 atm and gas temperatures of $T_g < 4000$ K, B_2N molecules dominate and their density outnumbers BN molecules by 2–3 orders of magnitude.³⁵ In addition, this work also presented the first experimental documentation of the emission by excited B_2N molecules in the visible spectrum, which was recorded in the laser ablation plume from a solid BN target. In the present paper, we are going beyond these initial studies of laser ablation of solid BN targets and focus on a comparison of gas phase reactions in the ablation plumes from boron and boron nitride targets. Here, we report the spatiotemporally resolved investigation of atomic and molecular emissions of the excited species in the ablation spectra of these solid targets in different gases such as N_2 , N_2 with admixed H_2 and He . In these experiments, the gas pressure was set at 500 Torr. The operation pressure is chosen to be comparable with BNNT synthesis conditions used in boron arc operation, described in ref. 19. Boron arcs were difficult to study due to their highly unstable and not well reproducible behavior and has a shorter runtime; therefore we have opted to study the chemical kinetics by OES during pulsed laser ablation, but under conditions similar to that of the arc. The addition of 10% H_2 to N_2 was meant to ease the plasma diagnostics *via* analysis of the H–Balmer series due to the reported contribution of H to an improved yield in the synthesis of BNNTs.²⁵ It was also suggested that species like NH and BH can be important intermediaries in the BNNT synthesis as their emission was detected when hydrogen was added to the thermal induction plasma (see ref. 25). Both of these species (BH and NH) were also predicted in the thermodynamic simulations,³⁵ therefore we were interested in investigating their formation. In addition, we also conducted experiments on ablation at much lower pressure of 100 mTorr. Our experiments revealed differences in the recorded spectra of the ablation plumes between the boron and BN targets. These results indicate the possible differences in the ablation mechanisms of these materials. In particular, it appears that the BN solid target favors the formation of large molecules such as B_2N . In order to support the analysis of emission dynamics we also measured the ablation rate of boron and boron-nitride targets and also carried out the characterization of plasma in

the ablation plumes, *via* investigation of atomic line broadening and intensity of different excitation stages of hydrogen atoms. One of the main objectives of this paper is to show and explain under which conditions, B_2N is formed and when it is not formed. The characterization of the plasma was conducted in order to allow basic estimations relevant to the formation of BN and B_2N molecules, and thereby facilitate the discussion on the formation of the molecular species.

2. Experimental setup and procedure

The experimental setup for the ablation consists of a stainless steel 6-way cross-equipped with four viewports allowing laser beam access through the window, into the chamber to the ablated target, and a view of the ablation plume in direction normal to the laser beam. The boron (rod-shaped ingot: 1 cm diameter, 2 cm height, and purity 99.5%) and boron-nitride (disc: 2.5 cm diameters, 5 mm thickness, and purity 99.5%) targets are situated on a 3D printed adapter tray, which is connected to a small, rotating electric motor. The ablation is driven by nanosecond laser pulses, provided by a Nd:YAG Continuum Surelite III laser. The fundamental harmonic of the laser frequency-tripled by a BBO crystal was used, generating 355 nm laser pulses with a full-width-at-half-maximum (FWHM) duration of ~ 5 ns and energy ~ 150 mJ. The laser beam is focused on the target with a lens, down to a ~ 200 μm spot, therefore the laser fluence is evaluated at ~ 120 $J\ cm^{-2}$ (irradiance ~ 15 $GW\ cm^{-2}$). Laser pulses are shot at a frequency of 10 Hz at the rotating target. The ablation plume is formed at the point of laser impact and extends in the horizontal direction (co-axial to the laser beam direction). The plume is imaged on the entrance slit of the imaging spectrometer (iHoriba 550). An ICCD camera (PIMax 3 by Princeton Instruments) is attached to the spectrometer, serving as a 2D signal detector. The plume image is rotated 90° by a Dove prism so that the plume length is imaged across the vertical direction of the ICCD. In this way, we have an ICCD image, where the horizontal axis corresponds to dispersion (represent the wavelength) and the perpendicular axis corresponds to the spatial distance in direction normal to the target. A BNC digital pulse delay generator was used to synchronize the operation of the laser with an iCCD camera. The initial exposure of the iCCD is timed to coincide with the end of the laser pulse. This is in order to avoid the saturation of the iCCD by the elastically scattered laser light and the strong continuum radiation right after the laser impact on the ablation target.

The sketch of the experimental setup is shown at Fig. 1. The emergence of the first spectral lines was observed with a spectrometer at approximately 10 ns after the end of the laser pulse. The data presented in this paper use the beginning of the observable laser pulse as the reference time ($t = 0$). The temporal evolution of the spectra was captured while increasing the delay of the iCCD camera acquisition up to few microseconds with respect to the laser shot. The intensity of the emission from different excited elements varied strongly between different species and at different delay times, therefore

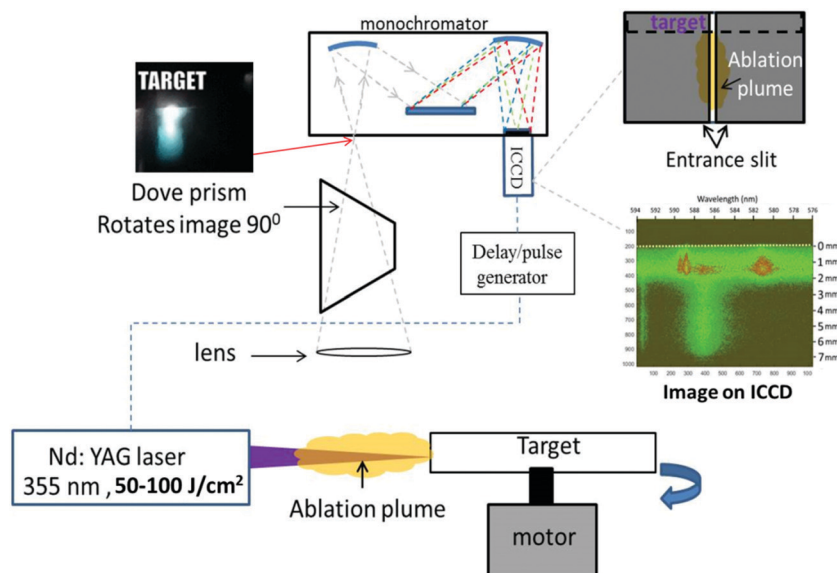


Fig. 1 Experimental setup for the optical emission spectroscopy study of laser ablation of B and BN targets.

capturing the emission of various elements required multiple accumulations at the same time delay. The exposures and the amount of accumulations vary between 20 and 500 ns for exposure and 50 and 800 accumulations. The approach of using accumulations relies on the assumption that the temporal evolution of chemical kinetics and plasma parameters are similar between the subsequent laser shots.

The spectra were obtained in the following two main configurations of the spectrometer. Spectral survey of the elements present in the discharge and the study of the emission intensity of various elements were conducted using the low resolution (150 g mm^{-1}) grating of the iHoriba spectrometer. To facilitate the analysis of plasma electron density we have added hydrogen (10% of total gas composition) to nitrogen gas. The line broadening of hydrogen Balmer α (H_{α}) line was measured using the low resolution grating in the first stages of the discharge, when the line profile was very broad. In the later stages of the discharge the line broadening of the H_{α} line was studied using the higher resolution grating (1200 g mm^{-1}). The spectral resolution and the instrumental broadening corresponding to the two gratings were measured using a calibration lamp (Oriel HgAr pencil lamp) and were determined to be $\Delta_{\text{instr}} \sim 0.7 \text{ nm}$ for 150 g mm^{-1} grating and $\Delta_{\text{instr}} = 0.079\text{--}0.038 \text{ nm}$ for 1200 g mm^{-1} grating. Finally, the transmission of the optical system for different spectral regions was calibrated with an integrated sphere light source (Labsphere URS-600).

3. Experimental results

3.1 Spectral survey and evolution of emission

We have examined the emission of the ablation plume in the visible spectrum (330–900 nm) during ablation of both boron and solid BN targets in low (100 mTorr) and high (500 Torr) pressures of helium and nitrogen gases. The identification of atomic lines relies on NIST database.³⁷ Emission of the BN(0,0)

band was detected in ablation of both BN and B targets (Fig. 2). BN emission was recorded in ablation of B and BN targets in 500 Torr of N_2 . In addition, BN emission was also observed when the BN target was ablated in 100 mTorr pressures. For both low- and high-pressure regimes, the ablation spectrum of the BN target also shows unidentified strong spectral features at ~ 362.15 , 362.8 and 364.2 nm . These features were also present in the results shown in the work of Dutouquet *et al.*³⁸ We hypothesized that these are molecular band-heads, due to the fact that these features remain visible up to $4 \mu\text{s}$ after the laser shot (at $P = 500 \text{ Torr}$). The emission of B_2N molecules was also observed. The identification of two B_2N band-heads was

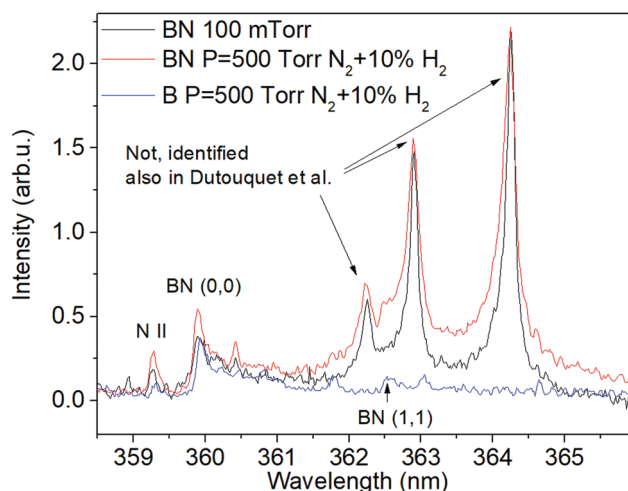


Fig. 2 Emission of BN molecules recorded during ablation of B and BN targets. Different color curves correspond to the different experimental conditions (ablated target and pressure). The emission intensities were normalized to fit a single plot, therefore they only reflect the relative emission intensity evolution as a function of time and are not to be compared between different species.

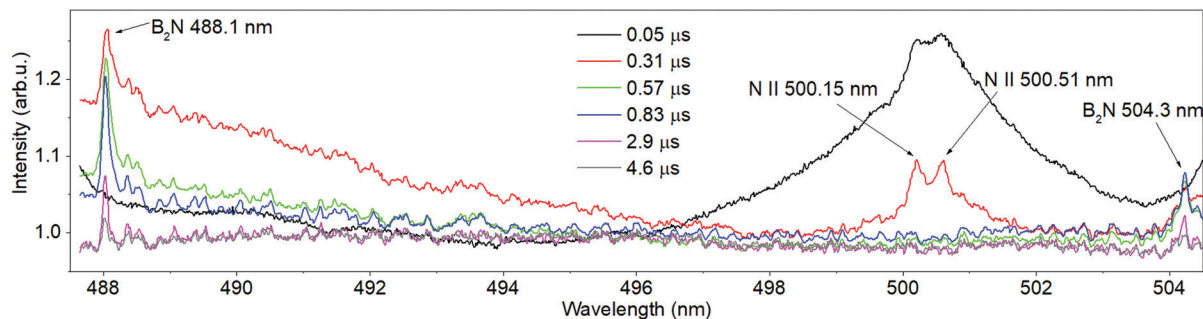


Fig. 3 Emission of B_2N molecular bands. Different color curves correspond to the spectra captured at different times with respect to the laser shot. Each curve was recorded under the same conditions and was not normalized, hence the signals represent the actual intensity of emission by the different species.

availed due to the calculated vibronic spectra of B_2N , presented in ref. 39. The evolution of the emission features in the spectral window shown in Fig. 3 includes both of these bandheads and the emission of several N II lines at 500–500.6 nm. The observed bandheads match the $\Sigma^1(0,1,0) - (0,1^1,0)$ and $\Delta^1(1,1,0) - (0,1^1,0)$ transitions of $^{11}B^{14}N^{11}B$ as postulated in ref. 39. The emission of N II in this spectral window serves as the reference for the identification of the B_2N bands. Finally, high-resolution spectra were recorded in the 470–530 nm region in order to detect other B_2N bandheads which were, for example, calculated by Ding *et al.*³⁹ The obtained results include various features with emission persisting for $t > 4 \mu s$ (at $P = 500$ Torr), but none of these results matched the rest of the B_2N bandheads indicated in ref. 39.

One of the interesting observations is that the ablation of the BN target showed both BN and B_2N emissions independent of the background gas and pressure, *i.e.* in a vacuum (100 mTorr), helium and nitrogen ($P = 500$ Torr). In contrast, the spectra recorded in the ablation plume from the boron target featured only BN(0,0) at 359.9 nm, while B_2N bandheads were not detected. This is despite the fact that these measurements were conducted with long exposures up to 400 ns and accumulations of up to 600 pulses.

Fig. 4 shows the temporal evolution of emission intensity from different atomic and molecular species in the ablation plume from BN and B targets. Here, the intensities were normalized to be shown together in the same plot. They represent the temporal evolution of emission by different species, but do not reflect the differences in their emission intensity. Fig. 4a shows the temporal evolution of emission in the ablation plume from BN target in a vacuum ($P = 100$ mTorr). In this case, the target serves as the source of generated species in the plume. The emission spectra of atomic species were recorded with an exposure to 20 ns, whereas the emission spectra of BN and B_2N molecules were recorded with an exposure to 50 ns. Under such conditions, the onset of emission by BN and B_2N molecules appears very early, at $t = 50$ ns, which is also when the maximum intensity of BN(0,0) emission is obtained. The peak of B_2N is slightly delayed, appearing at $t = 110$ ns. The emission from B and N ions also appears early at $t = 50$ ns and peak before 100 ns. The emission of neutrals

onsets later with respect to ions and molecules, reaching their peak at $t = 200$ ns. The time periods of first appearance and peak intensity of ions, neutrals and molecules are summarized in Table 1 for the different targets and pressures.

Another interesting observation shown in Fig. 4a is the apparent increase in the intensity of the BN(0,0) emission at $200 < t < 500$ ns, resulting in a local maximum around $t \sim 500$ –600 ns (indicated as stage III on the plot). The early emergence of BN and B_2N emissions is not exclusive to BN ablation in a vacuum and also observed in BN ablation in helium at $P = 500$ Torr. Fig. 4c compares BN and B_2N intensities for the ablation of BN targets in a vacuum (100 mTorr), helium, and nitrogen at $P = 500$ Torr. One can see that the helium and vacuum cases exhibit very similar evolution for BN and B_2N emissions, peaking at $t = 50$ ns and $t = 100$ ns, respectively. BN ablation in nitrogen is quite different, because both molecules reach peak intensity at much later stage, $t \sim 550$ ns. Fig. 4b and d depict the emission evolution following the ablation of boron (Fig. 4b) and BN targets (Fig. 4d) in nitrogen, where the emission of the ions was omitted to render the plots more readable. Note that in the case of boron targets (Fig. 4b), the signal was weak and observable only with a minimum exposure to 100 ns. It is evident that the temporal evolution of the emission of B, N and BN following the ablation of both targets is very similar, except the fact that no B_2N emission was detected in the ablation plume of the boron target Fig. 5 shows the spatially resolved spectra, including atomic species and B_2N bandheads, along the axis perpendicular to the surface of the target. Spatially, the emission of all elements, including molecules, starts adjacent to the target. The intensity is strongest at the vicinity of the target and extends to ~ 3 –4 mm away, during first 200 ns (see Fig. 5a). Fig. 5b shows two B_2N bandheads at $t = 1000$ ns, extending up to 7 mm. Here, the emission within the first mm of the target is gone. Our interpretation of these images is as the indication where the atomic species emitted by the target (and/or produced as a result of dissociation of molecules) participate in the reactions that produce the B_2N molecules in the volume bounded by the first ~ 3 mm adjacent to the target. In the later stages, the molecules diffuse further away from the target, reaching 7 mm away from the target. In Appendix B, we also present a collage of images that

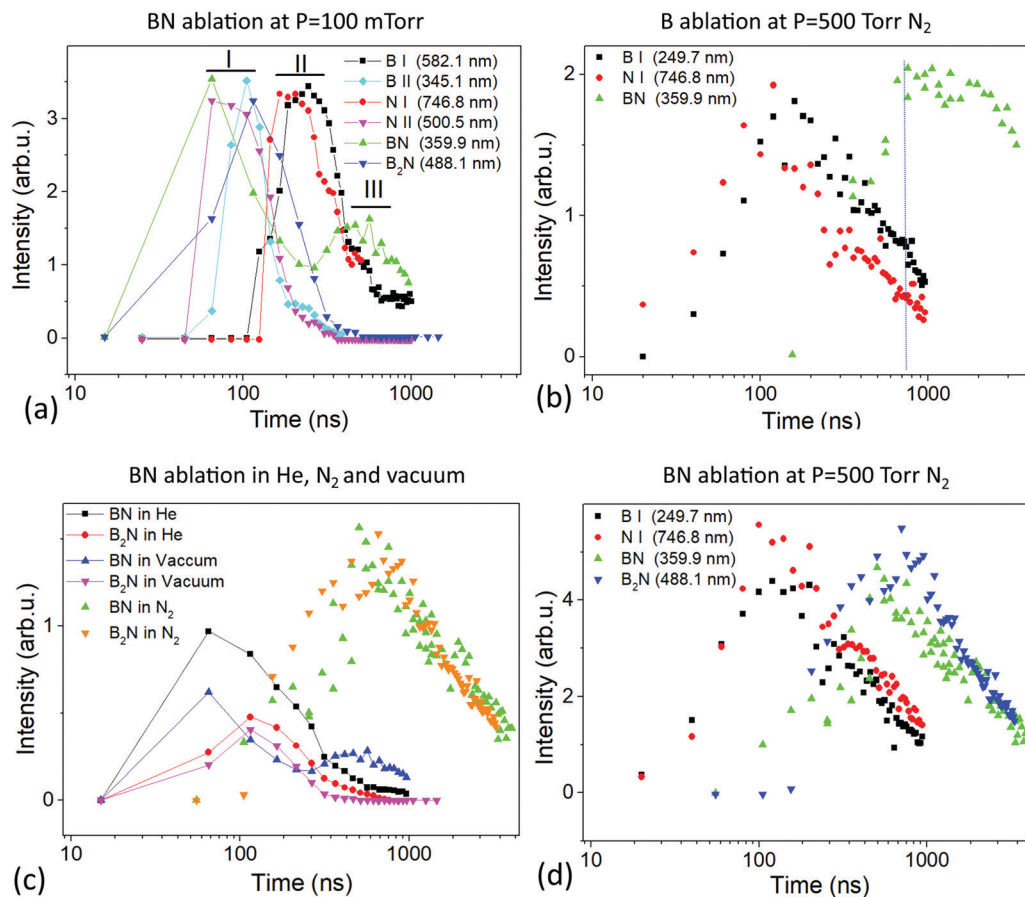


Fig. 4 Temporal evolution of the emission by different species. (a) Emission of atomic and molecular species following BN target ablation in a vacuum ($P = 100$ mTorr), phase I: peak emission of ions and molecules, phase II: peak emission of neutrals, phase III: secondary peaks of BN emission. (b) Emission of atomic and molecular species following B target ablation in 500 Torr of N_2 , the blue vertical line is added to indicate the apparent peak of BN emission. (c) Comparison of BN and B_2N emissions following BN target ablation in He, vacuum (100 mTorr) and N_2 . (d) Emission of atomic and molecular species following BN target ablation in 500 Torr of N_2 . The emission intensities were normalized to fit a single plot, therefore they only reflect the relative emission intensity evolution as a function of time and are not to be compared between different species.

Table 1 Timing of first appearance (t_0) and peak of intensity (t_{peak}) for ions, neutrals and molecular species in ablation plume of B and BN targets

Element/target material, pressure	B I time (ns)		B II time (ns)		N I time (ns)		N II time (ns)		BN time (ns)		B ₂ N time (ns)	
	t_0	t_{peak}	t_0	t_{peak}	t_0	t_{peak}	t_0	t_{peak}	t_0	t_{peak}	t_0	t_{peak}
B, 500 Torr	40	180	30	100	40	160	40	100	180	750	Not found	
BN, 500 Torr	40	180	30	100	40	150	30	100	115	600	120	800
BN, 100 mTorr	100	250	50	100	100	250	50	100	50	50 and 500	50	110

shows the spatial evolution of B and N ions lines in the first stages of ablation ($0 < t < 200$ ns).

3.2 Analysis of line intensities

Temporal evolution of intensities of the Balmer α and β lines was examined in order to probe the electron temperature T_e . The ratio of the line intensities, with wavelengths $\lambda_{p'q'}$ and λ_{pq} , is given by:⁴⁰

$$\frac{I(p \rightarrow q)}{I(p' \rightarrow q')} = \frac{\lambda_{p'q'} A_z(p \rightarrow q) g(p)}{\lambda_{pq} A_z(p' \rightarrow q') g(p')} \exp\left(-\frac{E(p) - E(p')}{k_B T_{ex}}\right) \quad (1)$$

where k_B is the Boltzmann constant, A is the Einstein coefficient of the transition, g is the degeneracy of the level and E is the energy of

the upper level in the transition, and $I(p \rightarrow q)$ and $I(p' \rightarrow q')$ are the intensities of the lines, corresponding to de-excitation from upper levels indexed by p, p' to lower levels indexed by q, q' , respectively. The excitation temperature T_{ex} is defined for a population of particles with Boltzmann distribution. Because of the exponential nature of this dependence, it is most sensitive when $k_B T_{ex} < E(p) - E(p')$. The upper level energy difference between H_α and H_β is ~ 0.66 eV, therefore that pair is best utilized for plasmas with $T_{ex} < 0.66$ eV. Under the assumption of thermodynamic equilibrium, the excitation temperature T_{ex} is equivalent to electron temperature T_e . Then, for the electron density, following Griem,⁴¹ the rate of electron collisions with the

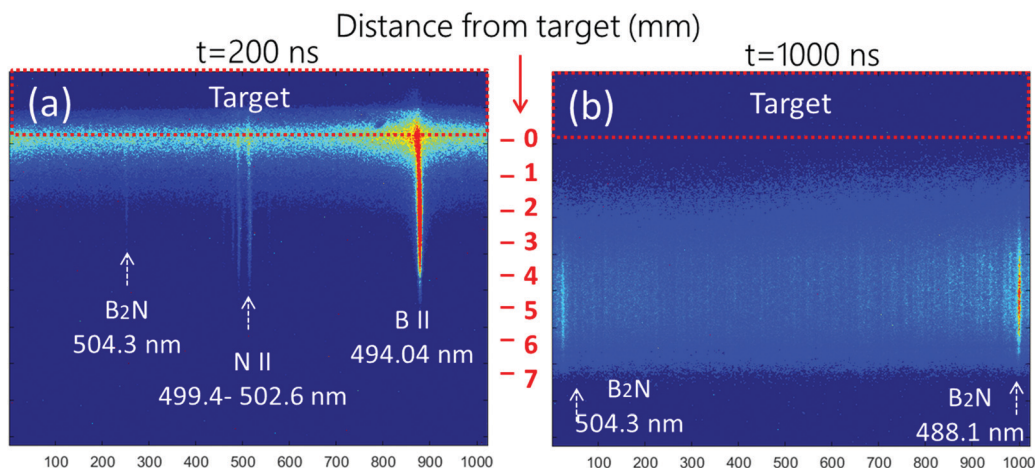


Fig. 5 ICCD images showing spectra captured during ablation of the BN target with spatial resolution in the direction "away from the target": (a) $t = 200$ ns, ionic lines and B_2N bandhead (b) $t = 1000$ ns, B_2N bandheads.

given species having the largest energy gap $[E(p) - E(q)]$ should be larger than radiative decay at least by a factor of 10:

$$\frac{n_e}{\text{cm}^{-3}} \geq 10^{14} \times \sqrt{\left(\frac{k_B T_e}{\text{eV}}\right) \left[\frac{E(p) - E(q)}{\text{eV}}\right]^3} \quad (2)$$

Since, our analysis of eqn (1) and (2) relies on the intensity of the lines; the opacity effect was evaluated using the following relationship:⁴¹

$$\tau(\lambda_0) = \pi r_e \lambda_0^2 f_{ik} n_i d \sqrt{\frac{M c^2}{2\pi k_B T_a}}, \quad (3)$$

where T_a is the temperature of the absorbing atoms, r_e (2.82×10^{-13} cm) is the classical electron radius, f_{ik} (0.641 and 0.119 for H_α and H_β respectively) is the absorption oscillator strength, λ_0 is the transition wavelength (656.3 and 486.1 nm for H_α and H_β respectively), $d = 0.5$ mm is the length of the absorbing homogeneous plasma slab, M is the atom mass (1.67355×10^{-24} g for hydrogen), n_i is the population density of the lower level, and c is the speed of light. The population density of the lower level in the transition is calculated using Boltzmann statistics, *i.e.* $n_i = N_a \exp\left(-\frac{E_i}{k_B T_a}\right)$, where density of absorbers N_a is calculated through a hydrogen atom percentage in the total gas mixture, assuming full dissociation of H_2 (for evaluation of the "worst case scenario", *i.e.* maximum amount of potential absorbers). The upper limit of the population is estimated for $T_a \approx T_e \sim 1$ eV and yields values $\tau(\lambda_0) \sim 10^{-5} - 10^{-6} \ll 1$, for H_α and H_β , safely rendering them as optically thin.

3.3 Analysis of line broadening

The spectra obtained in laser ablation experiments featured both H_α and H_β lines (see Appendix B). For the determination of the plasma density, H_α is more appropriate as its higher intensity gives a better signal-to-noise ratio (SNR). The emission of H_α appears ~ 20 ns earlier and lasts longer than that of H_β . Moreover, the H_β is much broader than H_α at the same plasma

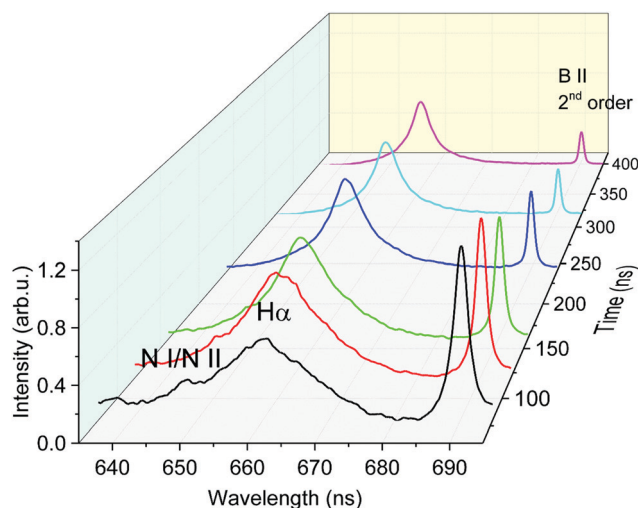


Fig. 6 Temporal evolution of the H_α line profile through first 400 ns after the laser shot.

density (N_e) and is hard to process. Although Balmer α line is also very broad in the first few hundreds ns, it is still possible to process and fit H_α profiles.

Fig. 6 shows the evolution of the H_α line at times $80 \leq t \leq 400$ ns, through several selected spectra recorded in that time interval during the ablation of a boron target. Spectral line broadening is caused by several mechanisms, such as instrumental broadening due to the finite resolution capability of the optical setup, Doppler broadening due to thermal motions of emitters, broadening due to collisions with neutral particles (van der Waals and resonance broadening) and the collisions with the charged particles (Stark). Stark broadening of spectral lines as a function of electron density (N_e) is conveniently tabulated, especially in the case of hydrogen lines.⁴² In order to obtain the Stark width of the spectral line one needs to de-convolute the rest of "widths" from the measured line profile. For moderate-high pressure plasmas, collisions between

Table 2 Instrumental, resonance, vdW, and Doppler broadening FWHMs of the H α line used for diagnostics

T_g (eV)	Δ_{Dopp} (nm)	Δ_{vdW} (nm)	Δ_{res} (nm)	Δ_{instr} (nm)
0.3	0.027	0.076	0.01	0.7 (g 150), 0.079–0.038 nm (g 1200)
0.6	0.04	0.096	0.01	0.7 (g 150), 0.079–0.038 nm (g 1200)

neutral particles can contribute significantly to the line broadening and need to be considered.⁴³ Instrumental broadenings for different spectrometer gratings were measured using calibration lamps. The upper limits for Doppler broadening and van der Waals (vdW) broadening are evaluated assuming that the gas temperature at its maximum approaches the electron temperature, *i.e.* $T_n = T_e$, where T_n is the temperature of neutrals. T_n is considered equivalent to the gas temperature T_g . The upper limit for resonance broadening is evaluated assuming maximum density of hydrogen atoms, *i.e.* full dissociation of the H $_2$ comprising 10% of 500 Torr gas pressure. Relevant calculations of the resonance broadening and vdW broadening were detailed in ref. 44. All broadening widths relevant to the described experiments are summarized in Table 2. It shows that broadening due to neutral collisions and Doppler broadening are negligible.

The experimental H α line profiles are fitted with Voigt profiles (*i.e.* convolution of Gaussian and Lorentzian), where the Gaussian contributions are due to the instrumental and Doppler broadening and Lorentzian is due to vdW, resonance and Stark broadening. In the current case, it is safe to assume the deconvolution of instrumental broadening from the experimental line one is left with Stark-broadened profile of the spectral line. Fig. 7 shows the calculated Voigt profiles compared with experimental H α profiles captured at $t = 80$ and 2000 ns. The full width-half maximum (FWHM) and full-width-half-area (FWHA) of hydrogen Balmer lines is tabulated as a function of N_e in the monumental work by Gonzales *et al.*,⁴² and was shown to depend very weakly on electron temperature T_e . In the same work, it is claimed that FWHA is a more stable parameter, therefore we used the diagnosis maps of H α FWHA for $\mu = 1$, found in supplemental materials. It should be noted that calibration expressions for FWHM and FWHA of Balmer series

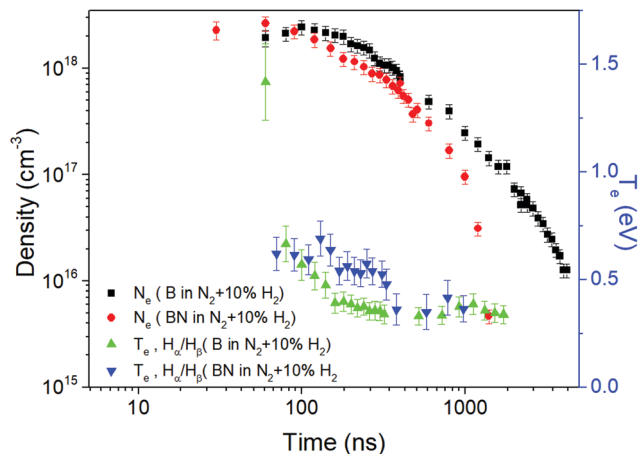


Fig. 8 Temporal evolution of the Ne and Te during ablation of B and BN targets in 500 Torr of N $_2$ + 10% H $_2$.

were derived in the same work and are very convenient for use⁴⁵ as opposed to diagnosis maps. However, we noticed that using the calibration expression (for H α FWHA) yields N_e larger by a factor ~ 2.6 than the values obtained from diagnosis maps. Therefore, we have opted to use the diagnosis maps, as a more particular approach.

Fig. 8 shows the temporal evolution of the electron temperature and the plasma density during the ablation for boron and BN targets in the N $_2$ + 10% H $_2$ ambient gas mixture at the pressure of 500 Torr. Since the emission of H β was observed at $t \geq 60$ ns, we could not deduce the excitation temperature from these measurements at earlier times. At later times, the electron temperature varies between 1 and 0.3 eV. This implies that the condition of eqn (2) is satisfied for the ablation of both boron and boron nitride targets with plasma densities of $n_e \geq 1.57$ and $2.88 \times 10^{13} \text{ cm}^{-3}$. With such high plasma densities reached at $t < 5 \mu\text{s}$, the local thermal equilibrium is satisfied and therefore we can refer to the temperature measured from the ratio of hydrogen Balmer lines as the electron temperature, rather than the excitation temperature.

For both boron and boron nitride targets, the plasma densities are comparable between $80 < t < 700$ ns (Fig. 8).

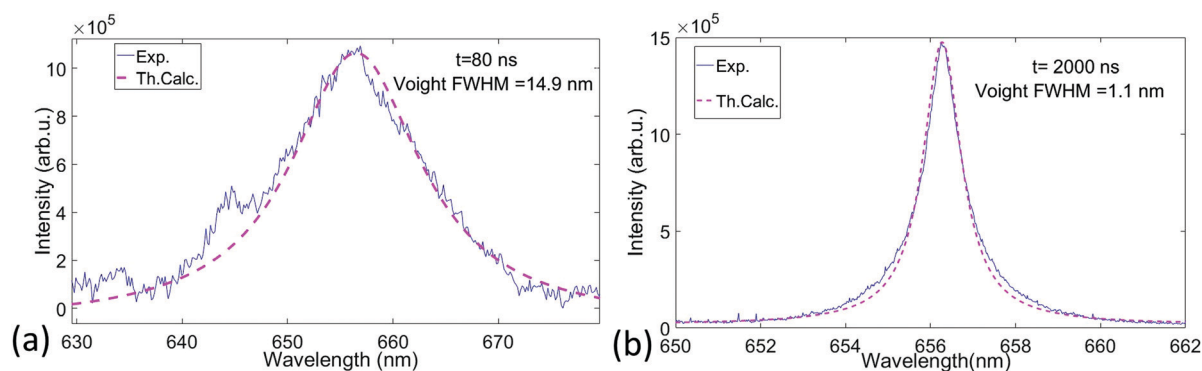


Fig. 7 Examples of experimental and fitted H α profiles obtained during B target ablation at $P = 500$ Torr N $_2$ + 10% H $_2$ (a) $t = 80$ ns, profile obtained with low resolution grating (150 g mm^{-1}) (b) $t = 2000$ ns, profile obtained with medium resolution grating (1200 g mm^{-1}).

In the case of the BN target, the plasma density decays quicker than that for the boron target after 700 ns. Furthermore, the Balmer series emission for the BN target disappears after 1100 ns, while for the boron target, both the H_{α} and H_{β} emission lines remain detectable up to $t = 5 \mu\text{s}$. With the earlier detection of Balmer lines for the BN target than for the boron target, the electron temperature for the BN target also shows a higher value around 0.6 eV at $t = 200$ ns and decreases down to 0.35 eV at $t \sim 500$ ns. For the boron target, the measured electron temperature remains nearly constant around ~ 0.35 eV for the whole period $300 < t < 1000$ ns.

Note that no significant differences in the line broadening/plasma density were found along the axis perpendicular to the target. The calculated densities and temperatures represent the averaged values across the whole plasma volume.

3.4 Quantification of ablated materials

In order to evaluate the amount of material ablated per laser shot we have conducted an experiment in which each target was weighted before and after a 10 min ablation experiment. For each target, the experiment was repeated 6 times in a vacuum ($P = 100$ mTorr) and in 500 Torr N_2 . We found no significant difference in the ablated weight of the target immersed in a vacuum ($P = 100$ mTorr) or high pressure ($P = 500$ Torr). Table 3 summarizes the ablation experiments in terms of the duration, number of laser pulses per experiment, ablated weight and corresponding density. For the boron target, we assumed that the ablated weight is comprised of only B atoms. For the case of BN targets, we assumed that the ablation is either by separate B and N atoms or by BN molecules (*i.e.* the ratio of ablated B and N is 1). The estimation of the ablation plume volume relies on

the spatial imaging of the emission lines (*e.g.* the propagation of the emission line edge with respect to the target edge, see Appendix B) and images of the ablation plume profile. Using the spatial imaging we estimate that within the ~ 40 ns after the laser pulse, the ablation plume can be approximated by a cylinder with a length of $\approx 0.2 \pm 0.03$ cm and a diameter of $\approx 0.1 \pm 0.03$ cm, *i.e.* a plume volume of $\approx 1.6 \text{ nm}^{-3}$. This volume is used in order to estimate the number density of the ablated species at the very early times following the laser pulse.

3.5 Plasma characterization

The following section analyses the case of ablation of B target, at nitrogen pressure $P = 500$ Torr. The measured plasma density and electron temperature in the case of BN target is very similar to the case of B target for $80 < t < 700$ ns, therefore, within this time range the discussion can be generalized to the BN case also. The laser ablation involves the evaporation of the target material, the formation of the plasma followed by the plasma decay. During these processes, the plasma density is determined by a trade-off between the plasma generation, plasma expansion (for ablation in a vacuum) and recombination. For the target ablation in collisional environments of the sub-atmospheric pressure ambient gas, the plasma generation and recombination govern the temporal evolution of the plasma density. An example of this evolution for the boron target under a nitrogen atmosphere ($P = 500$ Torr) is shown in Fig. 9. Here, the ionization degree (Fig. 9a) is defined as:

$$Z = \frac{N_c(t)}{N_n(t=0) - N_c(t)} \quad (4)$$

Table 3 Determining the weight and number density ablated from each target per laser pulse. The results are generalized for $P = 100$ mTorr and $P = 500$ Torr (nitrogen) cases, as no significant difference was found in the experiments

Target	Ablation experiment duration (s)	# of pulses	Total ablated mass (g^{-3}) ($P = 100$ mTorr and 500 Torr)	Ablated mass per shot (g^{-9}) ($P = 100$ mTorr and 500 Torr)	# of ablated B/B and N atoms	Ablation plume length (cm) at $t = 40$ ns	Number density (cm^{-3}) of ablated species
B	600	6000	0.15 ± 0.069	25	1.764×10^{16}	0.2	$(1.123 \pm 0.643) \times 10^{-19}$
BN	600	6000	0.29 ± 0.057	48.333	3.25×10^{16}	0.2	$(2.068 \pm 0.876) \times 10^{-19}$

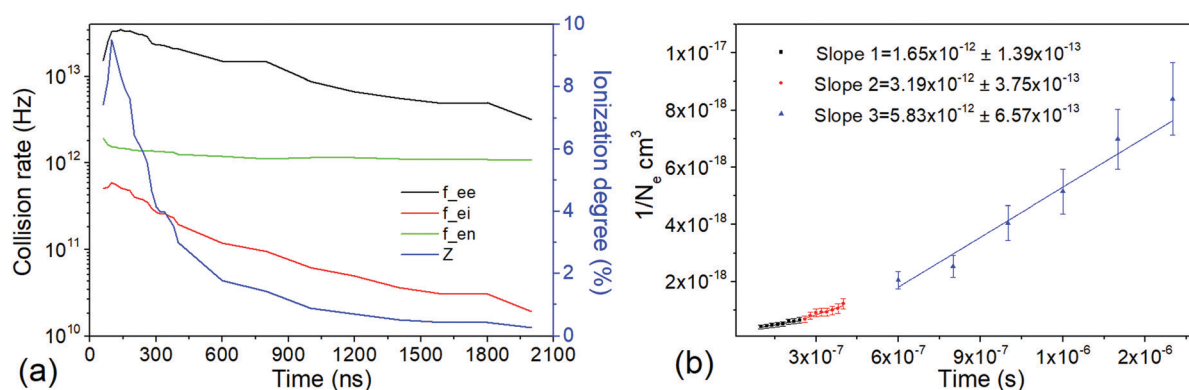


Fig. 9 Ablation of B target in gas ($P = 500$ Torr, 90% $N_2 + 10\%$ H_2). (a) Collision rates and ionization degree as a function of time (b) plot of $1/N_e$ in the time range of 100–2000 ns and linear fits of 3 time-segments of the curve.

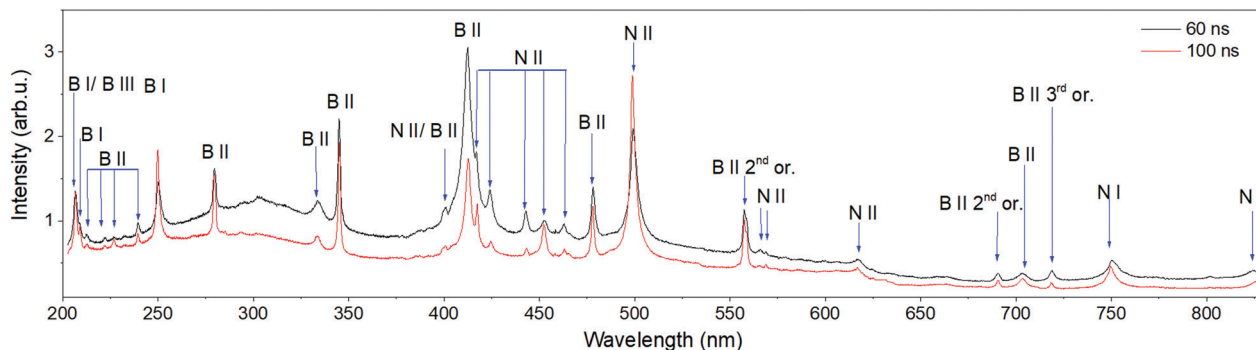


Fig. 10 Broadband spectral emission in the range of 200–830 nm for B ablation in N_2 . This spectrum is not corrected with the grating response function in order to preserve the readability of the figure. The apparent emission maximum at ~ 300 nm is because the spectrometer grating is blazed at 300 nm. No emission from N_2 or N_2^+ bands is observed. The camera gate time is 20 ns, and the spectrum is averaged over 10 accumulations.

In addition to the ionization degree, collision frequencies shown in Fig. 9a were calculated using measured N_e and T_e . The definitions of these frequencies are summarized in Appendix A. Apparently, our measurements captured the end of the processes where the plasma formation dominates over the recombination. The ionization degree initially increases reaching its peak value of 9% at 100 ns. This process is followed by the plasma decay when the ionization degree drops to $\gg 0.1\%$. During this plasma evolution, electrons are likely in thermal equilibrium between themselves as electron–electron collisions dominate over collisions of electrons with ions and neutrals. Because of a much higher density of the neutrals ($Z \ll 100\%$), elastic collisions of electrons with neutrals dominate over electron–ion collisions. These electron–neutral collisions contribute to the heating of atoms and molecules in the ablation plume (Appendix A).

According to Fig. 9, the plasma decay takes more than 2 microseconds. In the absence of an electric field, the charge densities decay with time according to

$$\frac{dN_e}{dt} = -\beta N_e N_i, \quad (5)$$

where β is the recombination coefficient. Here, we neglected the contribution of the plasma expansion in the reduction of the plasma density as it should not be a significant factor for the ablation in the surrounding gas (nitrogen or helium). The recombination coefficient can be determined experimentally via plotting N_e^{-1} as a function of time (Fig. 9a). From Fig. 9a, we find $\beta \approx 1.65 \times 10^{-12} \text{ cm}^3 \text{ s}^{-1}$ for $100 < t < 240$ ns, $\beta \approx 3.19 \times 10^{-12} \text{ cm}^3 \text{ s}^{-1}$ for $260 < t < 400$ ns, and $\beta \approx 5.83 \times 10^{-12} \text{ cm}^3 \text{ s}^{-1}$ for $600 < t < 1600$ ns.

The recombination can be governed by different mechanisms including radiative, dissociative and three-body processes, or their combination. It is instructive to determine which mechanism or mechanisms are dominant in the described ablation experiments. The radiative recombination ($A^+ + e^- \rightarrow A + h\nu$) coefficient is given by:⁴⁶

$$\beta_{rr} \approx 2.7 \times 10^{-13} (T_e [\text{eV}])^{-\frac{3}{4}} \text{ cm}^3 \text{ s}^{-1} \quad (6)$$

Dissociative recombination ($A_2^+ + e^- \rightarrow A + A^*$) relies on the presence of molecular ions. However, our measurements did

not record molecular ions in the emission spectrum (see Fig. 10). Furthermore, the value of dissociative recombination coefficient β_{dis} is $\sim 10^{-7} \text{ cm}^3 \text{ s}^{-1}$ for the temperature range from room to several thousand K,⁴⁶ decreasing as $\sqrt{T_e}$. Since in the present experiments, the measured plasma decay corresponds to $\beta \sim 10^{-12} \text{ cm}^3 \text{ s}^{-1}$, the dissociative recombination is apparently not relevant for the ablation plume from boron and boron nitride targets.

Finally, the three-body recombination ($A^+ + e^- + e^- \rightarrow A + e^-$) coefficient is given by:⁴⁶

$$\beta_{cr} \approx 8.75 \times 10^{-27} (T_e [\text{eV}])^{-\frac{9}{24}} n_e \text{ cm}^3 \text{ s}^{-1}. \quad (7)$$

Under the conditions of our experiments, this amounts to $\sim 10^{-8}$ – $10^{-7} \text{ cm}^3 \text{ s}^{-1}$ which is also much larger than the experimental values of $\beta \sim 10^{-12} \text{ cm}^3 \text{ s}^{-1}$.

Thus, the above analysis suggests that starting from $t > 100$ ns, the dominant recombination mechanism is radiative recombination. This may not be true for very early phases of the ablation (*i.e.* $t \leq 100$ ns), when ions recombine to produce neutrals and three-body recombination is the dominant mechanism. To demonstrate it we assume a simplified scenario in which neutrals are solely produced due to three-body recombination, so that the neutral density production rate is

$$\frac{dn_n}{dt} = \beta_{cr} \times n_i \times n_e. \quad (8)$$

Assuming that the plume plasma is quasi-neutral and taking the peak measured electron density we have $n_i = n_e = 1 \times 10^{18} \text{ cm}^{-3}$ and $\beta_{cr} \approx 1.1 \times 10^{-8} \text{ cm}^3 \text{ s}^{-1}$ (for $T_e = 0.5$ eV), corresponding to a neutral production rate of $\frac{dn_n}{dt} \approx 10^{28} \text{ cm}^{-3} \text{ s}^{-1}$. With such a high rate a density of $n_n \sim 10^{21} \text{ cm}^{-3}$ can be generated in a period of 100 ns. This simplified estimation shows that fast recombination due to three-body recombination can generate large neutral density on a scale of 100 ns, which is the delay between the observed peaks of ion and neutral emissions, during BN target ablation in a vacuum (Fig. 4a).

4. Discussion

4.1 Chemical kinetics: BN target in a vacuum and in He

The following section discusses the emission dynamics during ablation of the BN target, in order to understand the origin of BN and B₂N molecule formation. For the ablation of BN targets in helium and under vacuum, BN and B₂N emission peaks appear earlier than the emission peaks of B and N neutrals (Fig. 4a). This result suggests that the BN molecules originated either directly from the solid target or are formed in the very early stage of the ablation. This hypothesis is also supported by the spatial location of the molecular emission (BN and B₂N) that appears directly adjacent to the target (Fig. 5a). The emission of BN appears at the same time as the emission from B and N ions (Fig. 4a). The Einstein coefficients (A_{ki}) for the examined ion and neutral lines of B and N are similar (10^7 – 10^8 s⁻¹); nevertheless, the emission peaks of neutrals are delayed by >100 ns with respect to their ion counterparts. For example, for the N I 746.8 nm and N II 500.5 nm lines, the coefficients $A_{ki} = 1.96 \times 10^7$ s⁻¹ and 1.14×10^8 s⁻¹, respectively.³⁷ They correspond to natural lifetimes of ~51 and ~9 ns, respectively. Therefore, the delay between emissions of N I and N II, which are simultaneously excited by collisions with energetic electrons, should be ~40 ns. In a strongly collisional environment of the ablation-generated plasma, we can expect the effective lifetimes of the excited levels to be even shorter, and so should be their difference. In the experiment, however, the measured delay between the peak emissions of N I and N II is ~100 ns. Hence, one can conclude that the neutral population reaches its peak density later than ions by approximately 60 ns. Two possible scenarios can be considered to rationalize the lack of emission by neutrals in the early stage: (1) vast majority of ablated atomic species are ions and molecules (2) neutrals are rapidly consumed in the reaction that generates molecular species, before they can exhibit significant emission of their excited levels.

If scenario (1) is correct the ablated products should include BN and possibly B₂N molecules and B and N ions. Fast collisional quenching in the high density area makes the effective lifetimes of the excited vibronic levels to be short; our experiment shows emission within tens of nanoseconds as opposed to typical molecular natural lifetimes on the order of microseconds. In such circumstances, the peak emissions by ions and molecules appear within first 100 ns (Fig. 4a, phase I). The recombination of ions creates neutrals, whose intensity (and density) peaks are at $t \sim 250$ ns (Fig. 4a, phase II). Following the analysis and estimations done in Section 4.1, we can conclude that scenario (1) is plausible. The abundance of neutrals prompts a renewed formation of BN molecules, whose emission exhibits another peak at $t \sim 500$ ns (Fig. 4a, phase III). It has to be mentioned here that no correlation between BN and B₂N emissions was observed in this time range. Moreover, there is no late increase in the BN(0,0) emission during BN ablation in helium (Fig. 4c).

In scenario (2), it is hypothesized that the BN molecules are rapidly produced in the high density region which is formed immediately following the ablation near the target. In Section 3.4, we estimated that in the case of BN target ablation at $t = 40$ ns,

there would be a volume of ≈ 1.6 nm⁻³ occupied by B and N atoms or ions (here we assume that BN molecules are not emitted directly from the target). Then, the neutral density in this volume is $n = 2.07 \times 10^{25}$ m⁻³. Since the optical emission of ions is already observed at $t = 20$ ns, let us consider that the half of the ablated species are ions and half are neutrals, *i.e.* the number density of B and N neutrals is $n_{nB} = n_{nN} = 5.175 \times 10^{18}$ cm⁻³. Following ref. 47 the rate coefficient k for reaction $N + B + M \rightarrow BN + M$ was shown³⁵ to be 10^{-32} cm⁶ s⁻¹, where “M” represents all components in the system. In this case, the formation rate of BN: $\frac{dn_{BN}}{dt} = kn_{nB}n_{nN}n_M \approx 5.54 \times 10^{24}$ cm⁻³ s⁻¹. Thus, within 40 ns after the ablation starts, the density of BN molecules would amount to $\sim 2.22 \times 10^{17}$ cm⁻³. If all these molecules are excited, their density should be sufficient to exhibit emission. The considered reaction rate does not occur under isochoric conditions and relies on the above simplifications. Therefore, the above value constitutes a rough estimate. Nevertheless, it demonstrates that the outlined scenario is not completely far-fetched.

Note that a high BN density would also promote the rapid formation of B₂N molecules, *via* $BN + B + M \rightarrow B_2N + M$, resulting in slightly delayed emission peak of B₂N. The data that is currently available do not allow us to completely evaluate the viability of this scenario. A passive diagnostics approach such as OES is inherently limited in regards of investigating the chronological appearance of species on short timescales of few nanoseconds. Therefore, one would need to apply an active diagnostic approach for the measurement of existence and timing of appearance of B and N neutrals and BN molecular species.

To conclude this section, it appears that both the above-mentioned scenarios are plausible, based on rough estimations, although scenario (1) demands fewer assumptions and thus seems more probable than scenario (2).

4.2 Chemical kinetics: BN target in N₂ gas

The ablation of the BN target in N₂ gas is quite different from any other ablation case investigated in this work. For example, unlike ablation in helium and under vacuum, the BN ablation does not feature a peak of BN and B₂N emission within the first 100 ns. First recognizable signals from both molecules appear at $t = 100$ ns. The peak of BN(0,0) emission is reached at $t \sim 500$ ns, which is similar to the local maximum of BN(0,0) emission obtained for BN target ablation in a vacuum. This may be attributed to the BN formation by the B and N neutrals after both these species reach their density peaks (as manifested by peaks of optical emission, Fig. 4d, $t = 100$ ns).

4.3 Chemical kinetics: B target in N₂ gas

For the case of the boron target ablation in nitrogen, no emission of BN(0,0) is observed until $t = 350$ ns. The increase of the camera exposure to 100 ns did not help to detect BN emission. This is in contrast to the ablation of the BN target for which BN emission was observed right after the laser pulse with a camera exposure to 20 ns. A possible explanation of this result is that in order to form BN molecules, sufficient stocks of B and N species have to be built up in the plume. While boron is

abundant from the target, the nitrogen atomic species must be formed *via* dissociation of N_2 . It is generally acceptable that the dissociation of N_2 at moderate-to-high pressures (≥ 1.5 Torr) occurs mainly *via* vibrational excitation rather than by direct electron impact.^{48,49} Therefore, one would expect to see the emission from excited N_2 molecules. However, this is not the case in the described experiments because no emission from N_2 or N_2^+ was observed (see Fig. 10). The dissociation energy of the nitrogen molecule is 9.8 eV. It may be that a population of high energy electrons capable of dissociating N_2 is large enough before 50 ns (*i.e.* T_e is several eV), but not later, *i.e.* when we start measuring the temperature (≤ 1 eV) using the line emission ratio (eqn (1)). The same may be applied for step dissociation processes which are likely to take place in the collisional environment of the ablation plume ($\lambda_{\text{mfp}} \ll d, L$). It is likely that using active diagnostics for electron temperature (Thomson scattering) would be useful to measure the temperature before the emission from the necessary atomic lines appears. The reactions that do not involve dissociation of N_2 , *e.g.* ($N_2 + B \leftrightarrow BN + N$) have also been proposed.⁵⁰ However, to the best of our knowledge, there is no data available about this reaction and its rate. The viability of the dominance of this reaction may also be probed by using a laser induced fluorescence (LIF) approach to measure N_2 and boron densities and their dynamic behavior.

We also have to consider the possibility that the ablating material is pushing the ambient gas out, resulting in nitrogen deficiency and hence the late formation of BN molecules. Indeed, and estimation of the dynamic pressure in the expanding plume within first 40 ns is very high and would be certainly capable of pushing out the ambient gas. For the sake of discussion and evaluation we will assume that the material in the plume behaves as an incompressible fluid, in order to evaluate the “worst case scenario”. A simple evaluation of dynamic pressure for an incompressible fluid would be $q = \frac{\rho \times u^2}{2}$ [Pa], where $\rho = \frac{m \text{ [kg]}}{V \text{ [m}^3]}$ and u [m s⁻¹] are the mass density and the velocity of the expanding material, respectively. Relying on the ablation measurements in the paper we have $m = 25 \times 10^{12}$ kg, $u = 2.8 \times 10^4$ m s⁻¹ and $V = 1.6 \times 10^{27}$ m⁻³, giving $q = 6.125 \times 10^{24}$ Pa $\approx 4.6 \times 10^{22}$ Torr. This certainly will push out the ambient gas from the ablation plume area. Nevertheless, it is evident from the spectra obtained in times $t \leq 100$ ns, with B target in the N_2 gas: the emission of N ions and neutrals is featured at $t = 60$ ns (Fig. 10), therefore ambient N_2 is evidently found and is dissociated in the plume, possibly at the periphery of the plume. The fact that atomic N is only produced at the periphery of the plume may very well explain the “late” formation of BN, since it would take time to get the B atoms from the plume to occupy that region and react with the N atoms.

5. Conclusions

In this work, we presented the first integrated characterization of plasma properties (density and temperature) and chemical

reactivity during laser ablation of boron and boron nitride targets. The peak plasma density value is $\sim 10^{18}$ cm⁻³ (remaining so for ~ 200 ns following the laser pulse) and the measured peak electron temperature is ~ 1 eV (decreasing to ~ 0.3 – 0.4 eV after). The presence of B_2N molecules is manifested by the molecular emission of these species when the ablated target is BN, disregarding the background gas or lack of thereof. It is suggested that the BN and B_2N species are either emitted directly from the target or rapidly formed in the dense plasma region formed adjacent to the target during first tens of ns after the laser pulse. In order to decisively determine between these two scenarios an active diagnostics approach based on laser induced fluorescence could be used.

In the case of boron target ablation, the chemical kinetics in the ablation plume is different. Although atomic species emission behaves almost identically to the BN target case, the emission of BN molecules occurs much later (~ 300 ns), while no emission of B_2N is observed. The delay in the emission and alleged formation of BN is apparently due to the necessity to generate the feedstock of N atoms, which in the case of boron ablation under the N_2 atmosphere must come from the dissociation of nitrogen molecules. It is hypothesized that the formation of BN depletes the atomic N feedstock and therefore prevents a detectable production of B_2N molecules in the plume. We would also like to note that we have collected the synthesized material in all cases; however the material analysis is beyond the scope of this paper and is planned as a separate, future publication.

Thus, the laser ablation of the BN target promotes the formation of a larger variety of BN-based molecular species including both BN and B_2N compared to the ablation of the boron target under the nitrogen atmosphere which generates only BN molecules. This result may have a practical implication for the synthesis of BNNTs in plasmas. Specifically, the use of a solid BN ablation target or powder should enable a more efficient generation of boron and nitrogen feedstock for the synthesis of BNNTs than the ablation of the boron target or powder.

Conflicts of interest

There are no conflicts to declare.

Appendix A: calculation of collision frequencies and ionization degree

Electron–neutral collision rate:⁵¹

$$\nu_{\text{en}} = n_{\text{n}} \sigma_{\text{en}} \nu_{\text{eth}}, \quad (9)$$

where neutral density $n_{\text{n}} = \frac{P_{\text{g}}}{k_{\text{B}} T_{\text{n}}}$, $\sigma_{\text{en}} = 10^{-16}$ cm² electron–neutral collision cross section, and $\nu_{\text{eth}} = \sqrt{\frac{8k_{\text{B}} T_{\text{e}}}{\pi m_{\text{e}}}}$ thermal velocity of electrons.

Electron-ion collision rate:⁵¹

$$\nu_{ei} = 4.8 \times 10^{-8} n_i \text{ (cm}^{-3}\text{)} \times \ln \Delta \times T_i^{-\frac{3}{2}} \times \mu^{-\frac{1}{2}}, \quad (10)$$

where $\ln \Delta = 7.47 + 1.5 \times \log(T_e \text{ (K)}) - 0.5 \times \log(N_e \text{ (cm}^{-3}\text{)})$ ⁴⁶ is the Coulomb logarithm (~ 4 for our conditions) and $\mu = \frac{m_i}{m_p}$ is the ratio of ion mass to that of proton.

Electron-electron collision rate:⁵¹

$$\nu_{ee} = 2.9 \times 10^{-6} n_e \text{ (cm}^{-3}\text{)} \times \ln \Delta \times T_e^{-\frac{3}{2}}, \quad (11)$$

Here we have assumed quasi-neutrality of the plasma, *i.e.* $n_i = n_e$ and that $T_i \approx 4200$ K (evaporation temperature of B). Let us briefly discuss the validity of this assumption. The rate of ion heating by neutrals can be evaluated *via* $\frac{dT_i}{dt} = (T_e - T_i) \times \frac{2m_e}{M} f_{ei}$. For values $f_{ei} = 5.07 \times 10^{11} \text{ s}^{-1}$, $T_e \approx 1.06$ eV, $T_{i0} \approx 0.026$ eV (cold background gas) and $T_{i0} \approx 0.36$ eV (ablated material) we get $\frac{dT_i}{dt} = 4.085 \times 10^7 \text{ eV s}^{-1}$ and $2.75 \times 10^7 \text{ eV s}^{-1}$ for the cases of cold background gas and hot ablated material, respectively. Using these heating rates one can see that the ion temperature is very close to T_e after only 20 ns.

Appendix B: spectral lines spatial evolution and hydrogen Balmer series appearance

The time of flight of excited species can be evaluated *via* the imaging of species emission line evolution. Fig. 11 shows a

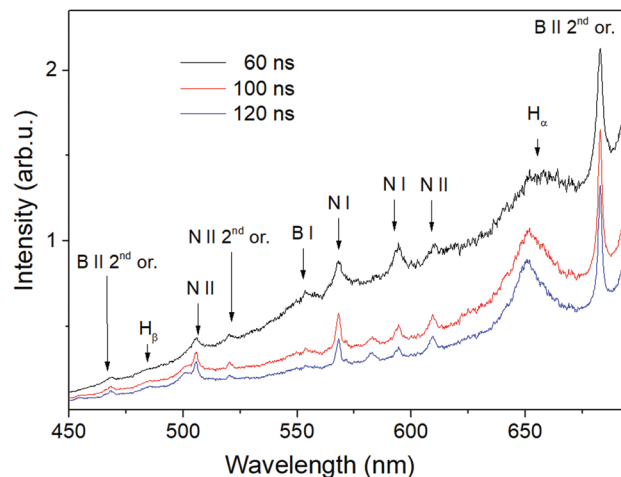


Fig. 12 Broadband emission featuring the first appearance of hydrogen Balmer α and β lines, during ablation of the B target in $N_2 + 10\%$ H_2 gas mixture. The spectrum was corrected for the grating response.

collage of images presenting the advancement of ion emission in the spectral range of 280–440 nm. The abscissa is the wavelength in nm and the ordinate is the distance from the target edge. The presented images are collected during the ablation of the solid BN target at pressure $P = 100$ mTorr. The velocity with which the front of ion emission proceeds is estimated to be $\sim 2.8 \pm 0.1 \times 10^6 \text{ cm s}^{-1}$ (using the bright emission of N II lines at 392 and 393 nm and B II emission at 412.2 nm).

Fig. 12 shows the broadband spectra in the range of 450–670 nm during ablation of the B target in a $N_2 + 10\%$ H_2

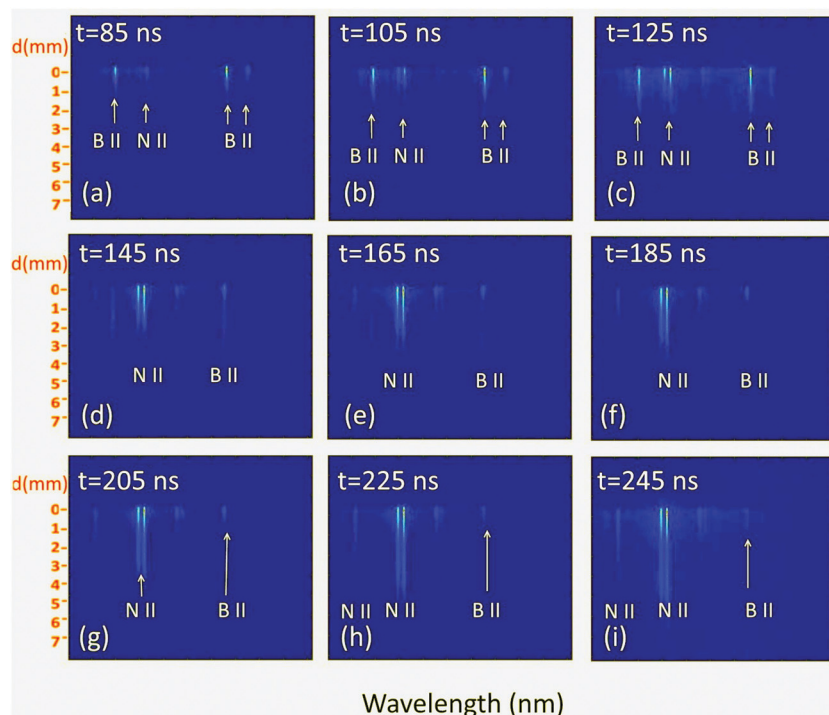


Fig. 11 Imaging the spectral line spatial evolution during the early period following the laser shot at the BN target at pressure $P = 100$ mTorr.

gas mixture, at pressure $P = 500$ Torr. The observed lines are indicated by species on the plot. As can be seen, in the plot, the peak of the Balmer β line starts to be distinguishable at about $t = 100$ ns and therefore this is when we can start “measuring” the temperature *via* the line intensity ratio.

Acknowledgements

The authors are grateful to Dr Igor Kaganovich, Dr Alexander Khrabry, Dr Rachel Selinsky, Dr Vladislav Vekselman, Dr M. Schneider and Dr Yuri Barsukov for fruitful discussion. The work on ablation of boron-rich materials was initiated under support by the US DOE, Office of Science, Basic Energy Sciences, Materials Sciences and Engineering Division. The material in this paper is based upon the work supported by the U.S. Department of Energy, Office of Science, Office of Fusion Energy Sciences under contract number DE-AC02-09CH11466.

References

- 1 A. Rubio, J. L. Corkill and M. L. Cohen, *Phys. Rev. B: Condens. Matter Mater. Phys.*, 1994, **49**, 5081–5084.
- 2 N. G. Chopra, R. J. Luyken, K. Cherrey, V. H. Crespi, M. L. Cohen, S. G. Louie and A. Zettl, *Science*, 1995, **269**, 966–967.
- 3 X. Chen, C. M. Dmuchowski, C. Park, C. C. Fay and C. Ke, *Sci. Rep.*, 2017, **7**, 11388–11397.
- 4 M. H. Bhuiyan, J. Wang, L. H. Li, P. Hodgson, A. Agarwal, M. Qian and Y. Chen, *J. Mater. Res.*, 2017, **32**, 3744–3752.
- 5 C. Zhi, Y. Bando, T. Terao, C. Tang, H. Kuwahara and D. Goldberg, *Adv. Funct. Mater.*, 2009, **19**, 1857–1862.
- 6 J. T. Grant, C. A. Carrero, F. Goeltl, J. Venegas, P. Mueller, S. P. Burt, S. E. Specht, W. P. McDermott, A. Chierregato and I. Hermans, *Science*, 2016, **354**, 1570–1573.
- 7 G. Elumalai, N. Noguchi and K. Uosaki, *Phys. Chem. Chem. Phys.*, 2017, **16**, 13755–13761.
- 8 N. Chejanovsky, Y. Kim, A. Zappe, B. Stuhlhofer, T. Taniguchi, K. Watanabe, D. Dasari, A. Finkler, J. H. Smet and J. Wrachtrup, *Sci. Rep.*, 2017, **7**, 14758–14772.
- 9 A. Pierret, L. Schue, F. Fossard, J. Barjon, O. Ersen, S. Moldovan, F. Ducastelle and A. Loiseau, European Microscopy Congress 2016, Proceedings, pp. 476–477.
- 10 R. Agrawal, A. Nietro, H. Chen and A. Agarwal, *ACS Appl. Mater. Interfaces*, 2013, **5**, 12052–12057.
- 11 X. Hong, D. Wang and D. D. L. Chung, *Composites, Part B*, 2016, **91**, 56–64.
- 12 J. H. Kang, G. Sauti, C. Park, V. I. Yamakov, K. E. Wise, S. E. Lowther, C. C. Fay, S. A. Thibeault and R. G. Bryant, *ACS Nano*, 2016, **9**, 11942–11950.
- 13 L. H. Li and Y. Chen, *Langmuir*, 2010, **26**, 5135–5140.
- 14 P. Ahmad, M. U. Khandaker and Y. M. Amin, *Ceram. Int.*, 2015, **41**, 4544–4548.
- 15 M. Ghazizadeh, J. E. Estevez and A. D. Kelkar, *Int. J. Nano Stud. Technol.*, 2015, **4**, 1–2.
- 16 V. Raffa, C. Riggio, M. W. Smith, K. C. Jordan, W. Cao and A. Cuschieri, *Technol. Cancer Res. Treat.*, 2012, **5**, 459–465.
- 17 G. Ciofani, V. Raffa, J. Yu, Y. Chen, Y. Obata, S. Takeoka, A. Menciasci and A. Cuschieri, *Curr. Nanosci.*, 2009, **5**, 33–38.
- 18 J. Cumings and A. Zettl, *Chem. Phys. Lett.*, 2000, **316**, 211–216.
- 19 Y. W. Yeh, Y. Raitses, B. E. Koel and N. Yao, *Sci. Rep.*, 2017, **7**, 3075–3082.
- 20 R. Arenal, O. Stephan, J.-L. Cochon and A. Loiseau, *J. Am. Chem. Soc.*, 2007, **129**, 16183–16189.
- 21 D. P. Yu, X. S. Sun, C. S. Lee, I. Bello, S. T. Lee, H. D. Gu, K. M. Leung, G. W. Zhou, Z. F. Dong and Z. Zhang, *Appl. Phys. Lett.*, 1998, **72**, 1966–1969.
- 22 L. C. Nistor, G. Epurescu, M. Dinescu and G. Dinescu, *IOP Conf. Ser.: Mater. Sci. Eng.*, 2010, **15**, 012067.
- 23 A. Fathalizadeh, T. Pham, W. Mickelson and A. Zettl, *Nano Lett.*, 2014, **14**, 4881–4886.
- 24 K. S. Kim, C. T. Kingston, A. Hrdina, M. B. Jakubinek, J. Guan, M. Plunkett and B. Simard, *ACS Nano*, 2014, **8**, 6211–6220.
- 25 K. S. Kim, M. Couillard, H. Shin, M. Plunkett, D. Ruth, C. T. Kingston and B. Simard, *ACS Nano*, 2018, **12**, 884–893.
- 26 B. Santra, H. Y. Ko, Y. W. Yeh, F. Martelli, I. Kaganovich, Y. Raitses and R. Car, *Nanoscale*, 2018, **10**, 22223–22230.
- 27 J. H. Kim, H. Cho, T. V. Pham, J. H. Hwang, S. Ahn, S. G. Jang, H. Lee, C. Park, C. S. Kim and M. J. Kim, *Sci. Rep.*, 2019, **9**, 15674–15684.
- 28 B. Stratton, A. Gerakis, I. Kaganovich, M. Keidar, A. Khrabry, J. Mitrani, Y. Raitses, M. Shneider, V. Vekselman and S. Yatom, *Plasma Sources Sci. Technol.*, 2018, **27**, 084001.
- 29 S. Yatom, J. Bak, A. Khrabry and Y. Raitses, *Carbon*, 2017, **117**, 154–162.
- 30 S. Yatom, A. Khrabry, J. Mitrani, A. Khodak, I. Kaganovich, V. Vekselman, B. Stratton and Y. Raitses, *MRS Commun.*, 2018, **8**, 842–849.
- 31 L. Han and P. Krstic, *Nanotechnology*, 2017, **28**, 07LT01.
- 32 P. Krstic, L. Han, S. Irle and H. Nakai, *Chem. Sci.*, 2019, **9**, 3803–3819.
- 33 N. R. Glavin, C. Muratore, M. L. Jespersen, J. Hu, T. S. Fisher and A. A. Voevodin, *J. Appl. Phys.*, 2015, **117**, 165305.
- 34 C. A. Thompson and L. Andrews, *J. Am. Chem. Soc.*, 1995, **117**, 10125–10126.
- 35 A. Khrabry, I. D. Kaganovich, S. Yatom, V. Vekselman, J. Radic-Peric, J. Rodman and Y. Raitses, *Phys. Chem. Chem. Phys.*, 2019, **21**, 13268–13287.
- 36 J. Radic-Peric, *Mater. Sci. Forum*, 2006, **518**, 349–354.
- 37 A. Kramida, Yu. Ralchenko, J. Reader and NIST ASD Team, 2019, NIST Atomic Spectra Database (ver. 5.7.1) [Online]. Available: <https://physics.nist.gov/asd> [2019, December 31].
- 38 C. Dutouquet, S. Acquaviva and J. Hermann, *Spectrochim. Acta, Part B*, 2005, **56**, 629–635.
- 39 H. Ding, M. D. Morse and J. P. Maier, *Mol. Phys.*, 2007, **105**, 1251–1261.
- 40 H. Kunze, *Introduction to Plasma Spectroscopy*, Springer-Verlag, Berlin, Heidelberg, 2009.
- 41 H. R. Griem, *Principles of Plasma Spectroscopy*, Cambridge University Press, Cambridge, 1997.

- 42 M. A. Gigosos, M. A. Gonzales and V. Cardenoso, *Spectrochim. Acta, Part B*, 2003, **58**, 1489–1504.
- 43 S. Yatom, E. Stambulchik, V. Vekselman and Ya. E. Krasik, *Phys. Rev. E: Stat., Nonlinear, Soft Matter Phys.*, 2013, **88**, 013107.
- 44 S. Yatom and Y. E. Krasik, *J. Phys. D: Appl. Phys.*, 2014, **47**, 215202.
- 45 S. Yatom, Y. Luo, Q. Xiong and P. J. Bruggeman, *J. Phys. D: Appl. Phys.*, 2016, **50**, 415204.
- 46 Y. P. Raizer, in *Gas Discharge Physics*, ed. J. E. Allen, Springer, Berlin, 1991.
- 47 Y. B. Zeldovich and Y. P. Raizer, *Physics of shock waves and high-temperature hydrodynamic phenomena*, ed. W. D. Hayes and R. F. Probstein, Academic Press, New York and London, 1966, vol. 1.
- 48 D. I. Slovetsky and R. D. Todesaite, *Sov. Phys., High Energy Chem.*, 1973, **7**, 291–297.
- 49 D. I. Slovetsky and R. D. Todesaite, *Sov. Phys., High Energy Chem.*, 1973, **7**, 297–305.
- 50 P. A. Gnoffo and C. C. Fay, *J. Thermophys. Heat Transfer*, 2013, **369**, 27–50.
- 51 J. D. Huba, *NRL Plasma Formulary*, 2016.